X International Conference on Computational Methods in Marine Engineering
MARINE 2023
J. García-Espinosa, L. González, J.E. Gutiérrez & B. Serván-Camas (Eds)

An Improved Direct Forcing Immersed Boundary Method for Simulating Floating Objects

Ahmet Soydan*, Widar W. Wang* and Hans Bihs*

* Department of Civil and Environmental Engineering,
NTNU Trondheim,
Høgskolereingen 7A,7491 Trondheim, Norway, web page: http://www.reef3d.com/
* Corresponding author: Ahmet Soydan, ahmet.soydan@ntnu.no

ABSTRACT

An enhanced direct forcing immersed boundary method implemented in the open-source hydrodynamic framework REEF3D::CFD is used to simulate six-degrees-of-freedom (6DOF) motion response of a 1:30 scale point-absorber wave energy converter(WEC) under extreme wave conditions. The enhancement of the method is achieved with a new density interpolation method that removes unphysical spurious phenomena. The governing equations are solved on a staggered rectilinear grid. REEF3D::CFD uses the level set function to represent the free surface. A ray casting algorithm is employed to get inside-outside information in the vicinity of the body with the underlying Cartesian grid. The enhanced method is tested and validated based on the experimental data from the experimental wave tank campaign carried out in the Ocean and Coastal Engineering Laboratory, at Aalborg University, in Denmark.

Keywords: CFD; REEF3D; 6DOF; floating bodies; free surface flow; level set method.

NOMENCLATURE

$\mathbf{g}$	Acceleration vector due to gravity
$\mathbf{u}$	Velocity vector
ρ	Density of the fluid
ν	Viscosity of the fluid
Φ	Signed distance funtion
$H(\Phi)$	Heaviside step function
$\mathbf{f}$	Forcing term
6DOF	Six degrees of freedom

1. INTRODUCTION

Accurate, efficient, and validated calculations of the fluid-floating object interactions are immensely challenging and of vital importance to computational fluid dynamics (CFD) based solvers. Immersed boundary method (IBM), as a non-boundary-conforming method, was initially introduced by Peskin (1972) to simulate fluid-structure interaction (FSI) problems associated with human heart valves. The method then has gained attention in recent years due to its simplicity and flexibility, and several variants of this method have been developed to improve its accuracy and enhance its applicability to realistic problems. Fadlun et al. (2000) introduced a direct formulation of the force term. In this method, the velocity boundary condition is imposed on a given immersed boundary. This scheme, called direct forcing, can be used with larger time steps contrary to Peskin's method. The earliest applications of the direct forcing method treat stationary bodies. When it comes to moving objects, spurious force oscillation occurs due to sudden changes in the relative position between the fixed grid and arbitrarily moving object. Uhlmann (2005) then combined the discrete delta function kernels with direct forcing formulations to resolve the spurious force oscillation problem. In this approach, the Eularian velocities at the fixed grid points are first interpolated to Lagrangian points on the immersed boundary via a regularized Dirac delta function. Then the local forcing term is calculated for corresponding desired velocity which depends on the boundary conditions on the fluid-solid body interface. Finally, the local forcing is transferred to surrounding Eularian locations using the regularized Dirac delta function. Similarly, this back-and-forth mechanism between Lagrangian and Eulerian locations to transfer the quantities is also used by Kempe & Fröhlich (2012); Kempe et al. (2015). In addition, Kempe et al. (2015) showed that even when the tangential force is set to zero, the standard direct forcing procedure leads to artificial shear stress at the fluid-solid body interface. Because the fluid velocity and viscosity are considered the same inside and outside of the immersed boundary. Therefore, an additional forcing was applied in the tangential directions and so the tangential velocity component could be modified. As a result, the shear stress at the solid body surface is set to zero, explicitly. Nevertheless, the smoothing process smear fluid-solid body interface and some ad hoc treatments implemented into IBM methods can lead to undesirable problems. In REEF3D::CFD, a ghost-cell immersed boundary method was initially implemented to represent the motion of the moving object (Kamath et al., 2017). Then, a continuous direct forcing method is implemented as a floating algorithm and it is currently used for fluid-floating object interaction problems.

In this paper, an enhanced direct forcing immersed boundary method in the open-source CFD code REEF3D::CFD (Bihs et al., 2016) is used for numerical calculations. The original implementation of a continuous direct forcing method in REEF3D::CFD (Martin et al., 2021) is improved with a new density interpolation method that removes unphysical spurious phenomena. The new implementation is validated with a 1:30 scale point-absorber wave energy converter (WEC) under extreme wave conditions. The numerical results are compared with numerical and experimental results.

2. NUMERICAL MODEL

2.1 Governing Equations

The conservation of mass and momentum which are written in convective form should be satisfied for an incompressible fluid.

$$\nabla \cdot \mathbf{u} = 0 \tag{1}$$

$$\frac{\partial \mathbf{u}}{\partial t} + \mathbf{u} \cdot \nabla \mathbf{u} = -\frac{1}{\rho}\nabla p + \nabla \cdot \left(\nu\left[\nabla \mathbf{u} + \nabla \mathbf{u}^T\right]\right) + \mathbf{g} \tag{2}$$

Here, **u** is the velocity vector, ρ is the density of the fluid, p is the pressure, ν is the sum of the kinematic and turbulent viscosity, and **g** the acceleration vector due to gravity. In REEF3D::CFD, the turbulence effect is taken into account by adding turbulent viscosity to the diffusion term using the Boussinesq approximation and a modified $k-\omega$ turbulence model (Bihs et al., 2016).

For the transition between the air and water phases, the level set function is (Osher & Sethian, 1988) used, which is defined as a signed distance function:

$$\Phi(\vec{x}, t) = \begin{cases} > 0 & \text{if } \vec{x} \in \text{phase 1} \\ = 0 & \text{if } \vec{x} \in \Gamma \\ < 0 & \text{if } \vec{x} \in \text{phase 2} \end{cases} \tag{3}$$

The Eikonal equation $|\nabla\Phi| = 1$ should also be satisfied in order to ensure mass conservation. A convection equation for the level set function

$$\frac{\partial\Phi}{\partial t} + \mathbf{u}\cdot\nabla\Phi = 0 \tag{4}$$

is solved using the fluid velocity field $\mathbf{u}$. The level set function is reinitialized after each time step to keep the signed distance properties. In REEF3D, a PDE based reinitializion equation is solved Sussman et al. (1994):

$$\frac{\partial\Phi}{\partial t} + \text{sign}(\Phi)\left(|\nabla\Phi| - 1\right) = 0 \tag{5}$$

where sign(Φ) is the smoothed sign function Peng et al. (1999). And then, the density and viscosity are calculated using

$$\rho = \rho_w H(\Phi) + \rho_a(1 - H(\Phi)) \tag{6}$$

$$\nu = \nu_w H(\Phi) + \nu_a(1 - H(\Phi)) \tag{7}$$

Here, w and a indicate water and air properties, respectively. The following Heaviside step function $H(\Phi)$ is used for smoothing of the sharp change of the fluid properties at the interface

$$H(\Phi) = \begin{cases} = 0 & \text{if } \Phi < -\epsilon \\ = \frac{1}{2}\left(1 + \frac{\Phi}{\epsilon} + \frac{1}{\pi}\sin\left(\frac{\pi\Phi}{\epsilon}\right)\right) & \text{if } |\Phi| \leq -\epsilon \\ = 1 & \text{if } \Phi < \epsilon \end{cases} \tag{8}$$

with an interface thickness of $\epsilon = 2.1\Delta x$.

The system of equations is solved using finite differences on a rectilinear staggered grid. A fifth-order accurate weighted essentially non-oscillatory (WENO) scheme (Jiang & Shu, 1996) is applied for the convection terms. The fifth-order accurate Hamilton-Jacobi WENO method of Jiang & Peng (2000) is used for discretization of the convection term in eq. (4). For diffusion terms, the second-order accurate central finite difference scheme is applied. An incremental pressure-correction algorithm (Timmermans et al., 1996) is used for the solution of the pressure gradient term in the RANS equation as described in Martin et al. (2021). In the predictor step, the conservation equation for momentum eq. (2) is solved without considering the pressure gradients. An intermediate velocity field $\mathbf{u}^{(*)}$ is calculated in each k-th Runge-Kutta sub-step using the following equation:

$$\frac{\mathbf{u}^{(*)} - \beta_k \mathbf{u}^{(n)}}{\alpha_k \Delta t} = \frac{1}{\Delta t}\mathbf{u}^{(k-1)} - \mathbf{u}^{(k-1)}\cdot\nabla\mathbf{u}^{(k-1)} - \frac{\nabla p^{(k-1)}}{\rho} + \frac{1}{\alpha_k}\nabla\cdot\left(\nu\left[\nabla\mathbf{u} + \nabla\mathbf{u}^T\right]\right)^{(*)} + \mathbf{g} \tag{9}$$

Here, α_k =1.0, 1/4, 2/3, β_k =0.0, 3/4,1/3 and k =1, 2, 3. The third-order accurate Total Variation Diminishing (TVD) Runge-Kutta scheme (Shu & Osher, 1988) is applied for the solution of the time derivatives as well as for eq. (4) and eq. (5). The time step size is controlled under the restriction of the CFL condition to ensure numerical stability efficiently. An implicit Euler method is applied for the time advancement of k and ω equations to prevent a significantly smaller time step size due to the CFL criterion. More detail can be found in Bihs et al. (2016). Diffusion term of the RANS equation is treated implicitly to remove their CFL restriction. The Poisson equation for the pressure of the new time step is formed by the insertion of the predicted velocities into the continuity equation.

$$\nabla\cdot\left(\frac{1}{\rho}\nabla p_{corr}\right) = \frac{1}{\alpha_k \Delta t}\nabla\cdot\mathbf{u}^{(*)} \tag{10}$$

The Poisson equation is solved for the pressure correction terms p_{corr} by the fully parallelized BiCGStab algorithm of the HYPRE library (van der Vorst, 1992) with the geometric multigrid pre-conditioner (Ashby

& Flagout, 1996) to increase the computational performance. Finally, the pressure and divergence-free velocity field are calculated using the following equations:

$$p^{(k)} = p^{(k-1)} + p_{corr} - \rho\nu\nabla \cdot u^{(*)} \tag{11}$$

$$\mathbf{u}^{(k)} = \mathbf{u}^{*} - \frac{\alpha_k \Delta t}{\rho}\nabla p^{(k)} \tag{12}$$

2.2 6DOF Algorithm

The fluid-structure interaction algorithm for the floating body in the REEF3D::CFD model is described in Martin (2021). The geometry of the floating body can be represented with an STL geometry consisting of multiple non-connected triangles. A ray casting algorithm (Bihs et al., 2017) is employed to get inside-outside information in the vicinity of the body. In the original approach, a signed distance function Φ_s can be generated. Eq. (6) and eq. (7) are extended to distinguish between fluid and solid domains as can be seen in Fig. 1.a. Here, s indicates the solid, and $H(\Phi_s)$ is used for representing the transition of the fluid to the solid.

$$\rho(\Phi,\Phi_s) = \rho_s H(\Phi_s) + (1 - H(\Phi_s)) \cdot (\rho_w H(\Phi) + \rho_a(1 - H(\Phi))) \tag{13}$$

$$\nu(\Phi,\Phi_s) = (1 - H(\Phi_s)) \cdot (\nu_w H(\Phi) + \nu_a(1 - H(\Phi))) \tag{14}$$

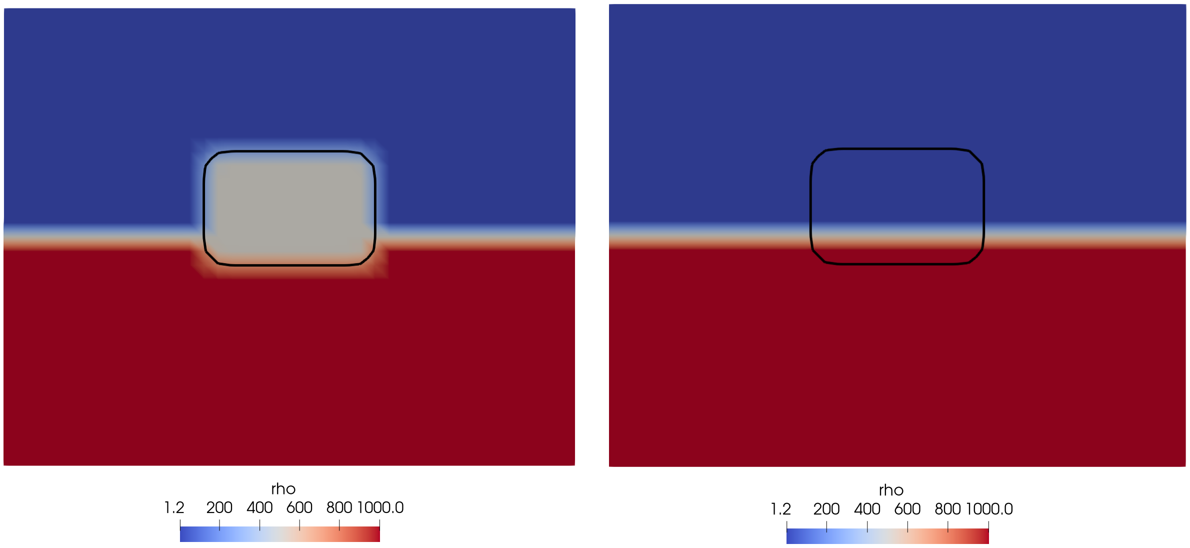

(a) Discontinuous solid density

(b) Continuous fluid density

Figure 1: Floating body density treatment

The original approach leads high-density gradient in the vicinity of the body. Therefore, the pressure field obtained by the Poisson equation would be unphysical. On the other hand, this approach needs quite refined cells around the solid body, and thus the thickness layer between the fluid and solid body should be relatively large to be able to keep stability. For this reason, the tangential velocity in the vicinity of the solid body can be problematic, and also the free surface sticks to the solid body and can not move freely. For this reason, the continuous fluid density treatment is implemented based on Eq. (6) and eq. (7) as can be seen in (Fig. 1.b). This approach provides an accurate pressure field and allows us to use relatively coarse cells around the body and a thinner thickness layer between the fluid and solid body. Hereby, calculation of the the tangential velocity around the solid body can be improved and the free-surface can move freely around the solid body.

A direct-forcing method is used to couple the solid and the fluid domains. The forcing field can be calculated by taking into account the conservation law as below.

$$\nabla \cdot \mathbf{u} = 0 \tag{15}$$

$$\frac{\partial \mathbf{u}}{\partial t} + \mathbf{u} \cdot \nabla \mathbf{u} = -\frac{1}{\rho} \nabla p + \mathbf{g} + \mathbf{f} \tag{16}$$

The additional source term (forcing term) **f** is included in the momentum equations to ensure the correct boundary conditions at the interface following the derivation in Yang (2018).

$$\mathbf{f} = \begin{cases} \frac{\partial \mathbf{P(u)}}{\partial t} + \mathbf{P(u)} \cdot \nabla \mathbf{P(u)} + \frac{1}{p} \nabla p - \mathbf{g} & \text{if } \Phi_s < 0 \\ \nabla \cdot \left(\nu \left[\nabla \mathbf{u} + \nabla \mathbf{u}^T \right] \right) & \text{if } \Phi_s > 0 \end{cases} \tag{17}$$

Here, **P(u)** projection operator is used to project the velocity field into a divergence-free rigid body velocity field. The forcing **f** at the new time step n+1 can be written in a discrete manner

$$\mathbf{f}^{(n+1)} = H\left(\Phi_s^{(n+1)}\right) \cdot \left(\frac{\mathbf{P}\left(\mathbf{u}^{(n+1)}\right) - \mathbf{P}\left(\mathbf{u}^{(n)}\right)}{\Delta t} + \mathbf{P}\left(\mathbf{u}^{(n)}\right) \cdot \nabla \mathbf{P}\left(\mathbf{u}^{(n)}\right) + \frac{1}{\rho} \nabla p^{(n+1)} - \mathbf{g} \right) \tag{18}$$

Pressure is taken from the previous time step and $\mathbf{P}\left(\mathbf{u}^{(n)}\right)) = \mathbf{u}^{(n)}$ is made as an approximation to be able to solve Eq.(18).

$$\mathbf{f}^{(n+1)} = H\left(\Phi_s^{(n+1)}\right) \cdot \left(\frac{\mathbf{u}^{(n+1)} - \mathbf{u}^{(n)}}{\Delta t} + \mathbf{P}\left(\mathbf{u}^{(n)}\right) \cdot \nabla \mathbf{u}^{(n)} + \frac{1}{\rho} \nabla p^{(n+1)} - \mathbf{g} \right) \tag{19}$$

Eq. 20 can be written by comparing with Eq. (9) and Eq. (19).

$$\mathbf{f}^{(n+1)} = H\left(\Phi_s^{(n+1)}\right) \cdot \left(\frac{\mathbf{P}(\mathbf{u}^{(n+1)}) - \mathbf{u}^*}{\Delta t} \right) \tag{20}$$

$\mathbf{u}^{(*)}$ itself can be chosen as the updated velocity field. Then, the calculation of the predictor step (9) is first performed without the forcing term. Therefore, $\mathbf{f}^{(*)}$ is calculated as below.

$$\mathbf{f}^{(n+1)} \approx \mathbf{f}^{(*)} = H\left(\Phi_s^{(*)}\right) \cdot \left(\frac{\mathbf{P}(\mathbf{u}^{(*)}) - \mathbf{u}^*}{\alpha_k \Delta t} \right) \tag{21}$$

After calculating the forcing term, it is added to the predicted velocity field. Then, the Poisson equation (10) is solved.

In order to obtain the rigid body velocity field, the transnational position of the rigid body $\mathbf{x}_i$ is defined in the inertia system, and the rotational motion is defined in a body-fixed coordinate system by means of the Euler parameter vector $\mathbf{e} = (e_0, e_1, e_2, e_3)^T$ with the property $\mathbf{e}^T\mathbf{e} = 1$. Tait-Bryan angles Φ, Θ, Ψ is used to define their relation as below (here,c is cosine function and s is sine function) (Goldstein et al., 2001)

$$\begin{aligned}
e_0 &= c\left(\frac{\Phi}{2}\right) \cdot c\left(\frac{\Theta}{2}\right) \cdot c\left(\frac{\Psi}{2}\right) + s\left(\frac{\Phi}{2}\right) \cdot s\left(\frac{\Theta}{2}\right) \cdot s\left(\frac{\Psi}{2}\right) \\
e_1 &= s\left(\frac{\Phi}{2}\right) \cdot c\left(\frac{\Theta}{2}\right) \cdot c\left(\frac{\Psi}{2}\right) - c\left(\frac{\Phi}{2}\right) \cdot s\left(\frac{\Theta}{2}\right) \cdot s\left(\frac{\Psi}{2}\right) \\
e_2 &= c\left(\frac{\Phi}{2}\right) \cdot s\left(\frac{\Theta}{2}\right) \cdot c\left(\frac{\Psi}{2}\right) + s\left(\frac{\Phi}{2}\right) \cdot s\left(\frac{\Theta}{2}\right) \cdot s\left(\frac{\Psi}{2}\right) \\
e_3 &= c\left(\frac{\Phi}{2}\right) \cdot c\left(\frac{\Theta}{2}\right) \cdot s\left(\frac{\Psi}{2}\right) - s\left(\frac{\Phi}{2}\right) \cdot s\left(\frac{\Theta}{2}\right) \cdot c\left(\frac{\Psi}{2}\right)
\end{aligned} \tag{22}$$

The back-transformations are calculated as

$$\begin{aligned}
\Psi &= \text{arctan2}(2 \cdot (e_1 \cdot e_2 + e_3 \cdot e_0), 1 - 2 \cdot (e_2 \cdot e_2 + e_3 \cdot e_3)) \\
\theta &= \arcsin(2 \cdot (e_0 \cdot e_2 + e_1 \cdot e_3)) \\
\phi &= \text{arctan2}(2 \cdot (e_2 \cdot e_3 + e_1 \cdot e_0), 1 - 2 \cdot (e_1 \cdot e_1 + e_2 \cdot e_2))
\end{aligned} \tag{23}$$

A vector in the body-fixed coordinate system is transformed to a corresponding vector in the inertial system by means of the orthogonal rotation matrix

$$\mathbf{R} = 2\begin{pmatrix} \frac{e_0^2+e_1^2-e_2^2-e_3^2}{2} & e_1 e_2 - e_0 e_3 & e_0 e_2 + e_1 e_3 \\ e_0 e_3 + e_1 e_2 & \frac{e_0^2-e_1^2+e_2^2-e_3^2}{2} & e_2 e_3 - e_0 e_1 \\ e_1 e_3 - e_0 e_2 & e_0 e_1 + e_2 e_3 & \frac{e_0-e_1^2-e_2^2+e_3^2}{2} \end{pmatrix} \tag{24}$$

The kinematic equations for the rotational motion of the rigid body in respect of the Euler parameters are defined as

$$\dot{\mathbf{e}} = \frac{1}{2}\mathbf{G}^T\omega \tag{25}$$

Here, ω is the angular velocity vector in the body-fixed coordinate system.

$$\mathbf{G} = \begin{pmatrix} -e_1 & e_0 & e_3 & -e_2 \\ -e_2 & -e_3 & e_0 & -e_1 \\ -e_3 & e_2 & -e_1 & e_0 \end{pmatrix} \tag{26}$$

Eq. (25) can be revised by putting the momentum vector $\mathbf{h} = \mathbf{I}\omega$ with $\mathbf{I}$ the moment of inertia tensor into the Eq. (25) as

$$\dot{\mathbf{e}} = \frac{1}{2}\mathbf{G}^T\mathbf{I}^{-1}\mathbf{h} \tag{27}$$

A first-order ODE is derived for $\dot{\mathbf{h}}$ using a system Hamiltonian (Shivarama & Fahrenthold, 2004). The equation can be written by forcing the potential energy function to zero and imposed moments $\boldsymbol{M_b}$ in the body-fixed system as

$$\dot{\mathbf{h}} = -2\mathbf{G}\dot{\mathbf{G}}^T\mathbf{h} + M_b \tag{28}$$

The moments in the body-fixed system $\boldsymbol{M_b}$ are obtained from the inertia system by means of the transformation matrix (24).

The translational motion of the rigid body is defined by Newtons second law as below and converted to a first-order differential equations system.

$$\ddot{\mathbf{x}}_s = \frac{\mathbf{F}_i}{\rho_s V} \tag{29}$$

The position and the velocity of the centre of gravity can be calculated by integrating Eq. (29). Overall,Eqs. (29), (25) and (28), a system of thirteen first-order ODEs comes up. The system is integrated with the same explicit scheme as the fluid solver.

The body forces and momenta are calculated by integrating the fluid properties (pressure p, the viscous stres tensor τ) over the solid surface Ω.

$$F_i = \int_\Omega (-\mathbf{n}p + \rho\nu\mathbf{n}\tau)d\Omega(\mathbf{x}) = \sum_{i=1}^{N}(-\mathbf{n}p + \rho\nu\mathbf{n}\tau)_i \cdot \Delta\Omega_i \tag{30}$$

$$M_i = \int_\Omega \mathbf{r} \times (-\mathbf{n}p + \rho\nu\mathbf{n}\tau)d\Omega(\mathbf{x}) = \sum_{i=1}^{N}\mathbf{r}_i \times (-\mathbf{n}p + \rho\nu\mathbf{n}\tau)_i \cdot \Delta\Omega_i \tag{31}$$

where $\mathbf{n}$ is the surface normal vector on the solid body surface pointing outwards, and $\mathbf{r}$ is the distance vector to the body's centre of gravity. By using the transformation matrix (24), the moments are transferred to the body-fixed coordinate system. After calculating body velocities, the projection can be calculated by using Eq. (32)

$$\mathbf{P}\left(\mathbf{u}^{(*)}\right) = \dot{x}_i + \omega_i \times r \tag{32}$$

where $\dot{x}_i$ is the translational rigid body velocity vector and ω_i is the rotational rigid body velocity vector in the inertial reference frame.

3. RESULTS

For testing the new implementation of a direct-forcing immersed boundary method, the motion responses of a 1:30 scale point-absorber wave energy converter (WEC) under extreme wave conditions are simulated.

The simulation conditions are taken into account based on the study of Katsidoniotaki et al. (2023). In that work, the open-source CFD code OpenFOAM-v1906 is used. This code solves the three-dimensional RANS equation using the finite volume method and free-surface is modeled with the volume of fluid method. The motion of the rigid body is handled with the dynamic mesh method. Two different wave steepness are considered as 0.068 and 0.035 (Table 2) in that study. The experimental results are taken from Shahroozi et al. (2022). The physical properties of the buoy are given in Table 1. The simulation domain of the numerical wave tank (NWT) is generated with dimensions 24.42 m x6.0 m x 3.0 m. 0.1 m grid size is applied for the computational domain and grid stretching is applied around the body and the free-surface in order to represent properly which can be seen in Fig. 2. The grid size around the body and free-surface is 0.025 m.

Table 1: Physical properties of the buoy

Parameters	Unit	Value
Diameter	m	0.33
Height	m	0.38
Draft	m	0.23
Mass	kg	15.73
Center of gravity	m	(0.0, 0.0, 0.1186)
Moment of inertia	kgm^2	(0.3537, 0.3537, 0.2918)

The numerical wave tank (NWT) length is chosen depending on the wavelength. Several wave generation and absorption methods are included such as a relaxation method, a Dirichlet-type method, and a active wave absorption method within REEF3D numerical framework Miquel et al. (2018). In this study, the relaxation method is used for both the wave generation and absorption and the wave generation & absorption beach is equivalent to one wavelength and two wavelengths, respectively. 2nd-order Stokes theory is used for the waves. The wave is generated in the wave generation zone and absorbed in the absorption beach as can be seen in Fig. 3. CFL number is set as 0.1 for numerical calculations.

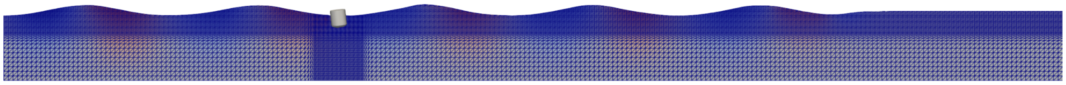

Figure 2: Surface of the NWT, showing the grid stretching around the structure and free-surface

Table 2: Wave Characteristics

Sea state	H [m]	T [s]	λ[m]	H/λ [-]
9	0.22	1.52	3.20	0.068
10	0.115	1.52	3.20	0.035

The mooring force is modeled by a simpler linear spring equation to reproduce the sum of the forces produced by the PTO, the pulleys, and the damping force due to the translator in the experiment. Details about the PTO system can be found in (Katsidoniotaki et al., 2023; Shahroozi et al., 2022).

$$F = F_0 + k \cdot \delta l \tag{33}$$

In the Eq. 33, F_0 is the pretension of the spring, k is the linear spring stiffness coefficient and δl is the extension of the spring.

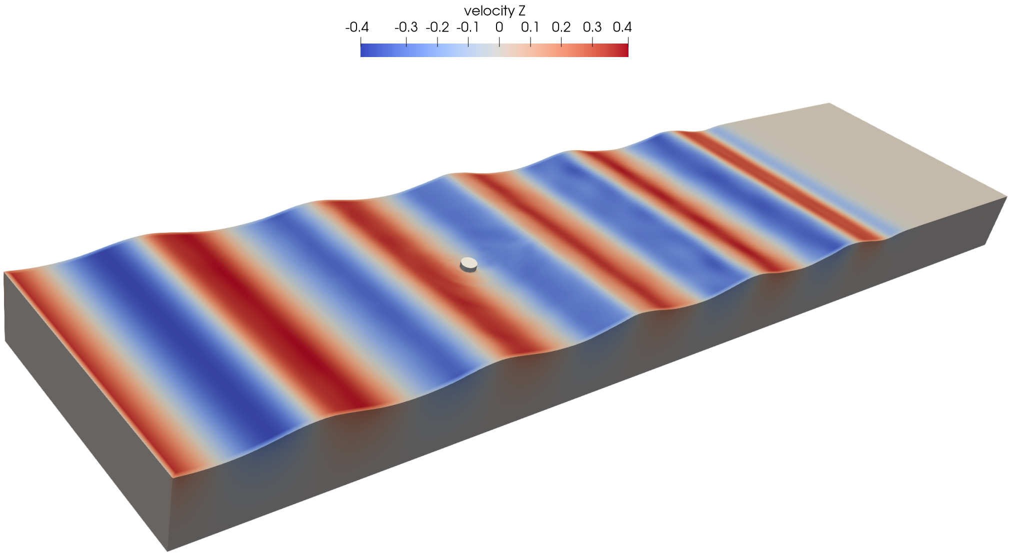

Figure 3: Vertical velocity distribution on the-free surface

The time series of the motion responses for WEC is presented Fig. 5 with the experimental results and the numerical results in Katsidoniotaki et al. (2023). Fig. 4 shows the WEC's motion response under the wave conditions of RW9 during a wave period. The peaks of the heave results of REEF3D::CFD shows a good agreement between numerical results and experimental data in Fig. 5 a and b. On the other hand, the troughs of the numerical results are overestimated contrary to underestimated numerical results in Katsidoniotaki et al. (2023). The surge motion shows an offset between numerical results and experimental data similar to the results in Katsidoniotaki et al. (2023). Nevertheless, the phase of the surge and heave motion match the experimental measurement well. When it comes to pitch motion, the numerical results do not match the experimental data and show a larger deviation. As mentioned in Katsidoniotaki et al. (2023), the validation study was not carried out during the experiment to determine the buoy characteristics such as the center of gravity, the center of rotation, and moment of inertia. These physical properties obtained from the CAD model might cause some deviation from the exact values and it can affect the pitch motion result which is more sensitive to the change of these parameters.

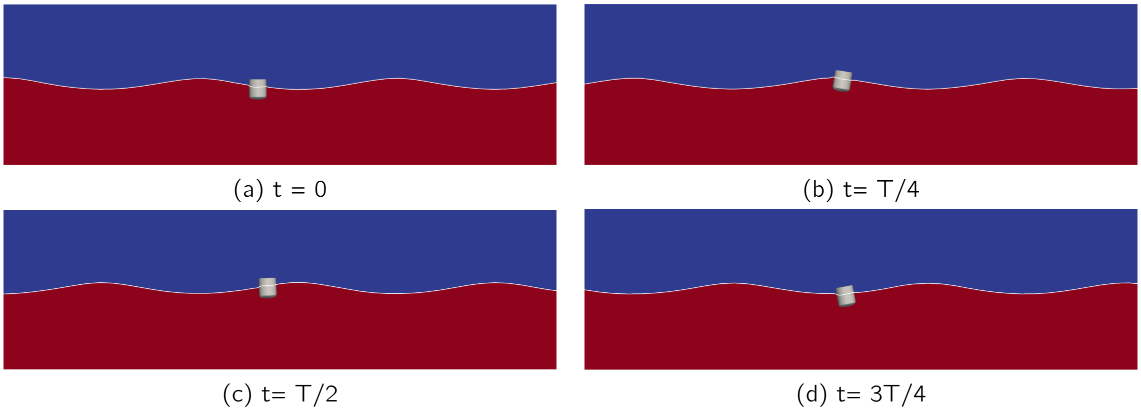
(a) t = 0

(b) t= T/4

(c) t= T/2

(d) t= 3T/4

Figure 4: WEC's motion response under the wave condition of RW9.

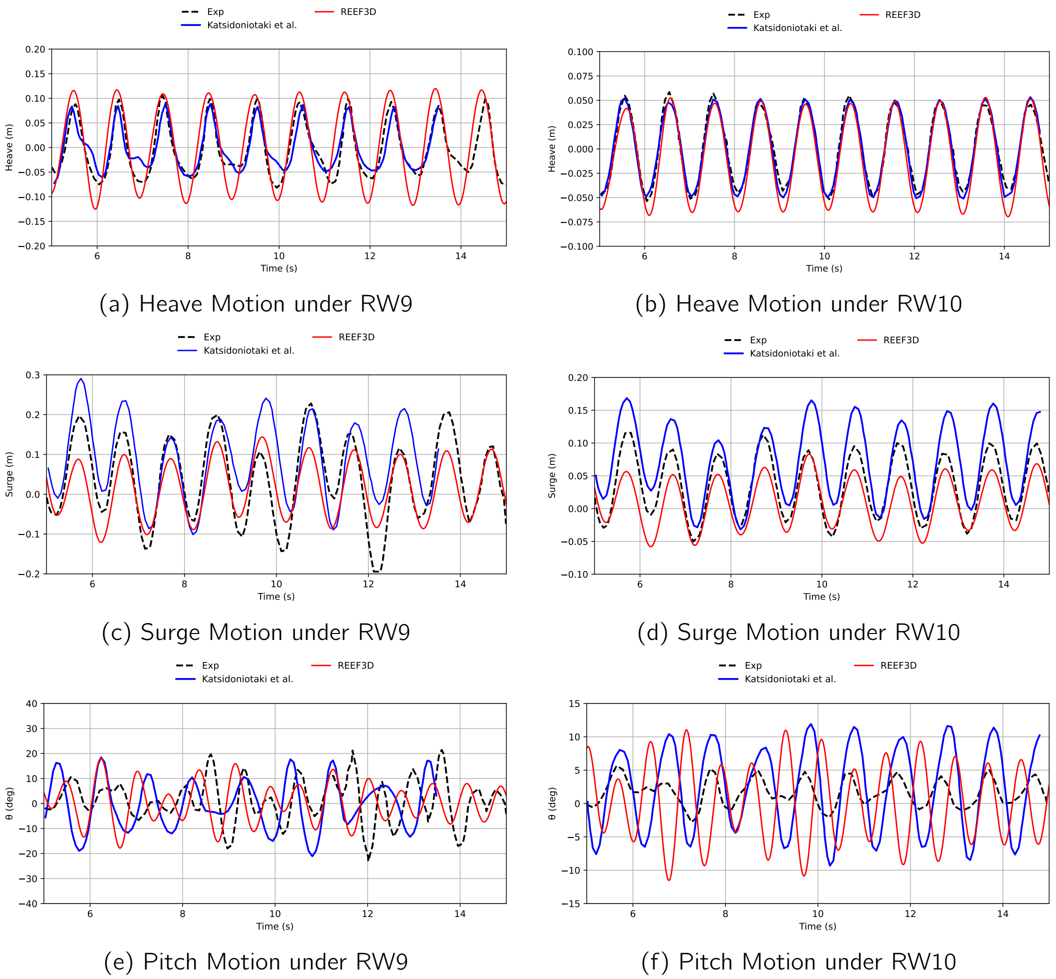

(a) Heave Motion under RW9

(b) Heave Motion under RW10

(c) Surge Motion under RW9

(d) Surge Motion under RW10

(e) Pitch Motion under RW9

(f) Pitch Motion under RW10

Figure 5: Time series of motion responses for WEC.

4. CONCLUSIONS

An enhanced direct forcing immersed boundary method implemented in REEF3D::CFD has been introduced and tested with a 1:30 scale point-absorber WEC under extreme wave conditions. The heave motion results of REEF3D::CFD shows good agreement with the experimental data and the numerical results in (Katsidoniotaki et al., 2023). An offset is observed in the surge motion results, but the phase of the surge and heave motions match well with the experimental results. In the pitch motion, there are high deviations between numerical and experimental results. This may be due to the uncertainty of the physical properties of the buoy. More studies are needed to assess this problem. For further studies, the irregular focused wave conditions will be covered.

ACKNOWLEDGEMENTS

The authors are grateful for the grants provided by the Research Council of Norway under the IPIRIS project (no. 308843). The simulations were performed on resources provided by Sigma2 - the National Infrastructure for High Performance Computing and Data Storage in Norway.

References

Ashby, S., & Flagout, R. (1996). A parallel mulitgrid preconditioned conjugate gradient algorithm for groundwater flow simulations. *Nuclear Science and Engineering*, *Volume 124(1)*, 145–159.

Bihs, H., Kamath, A., Alagan Chella, M., & Pakozdi, C. (2017). Complex geometry handling for a cartesian grid based solver. In *MekIT'17-Ninth national conference on Computational Mechanics*. International Center for Numerical Methods in Engineering (CIMNE).

Bihs, H., Kamath, A., Chella, M. A., Aggarwal, A., & Arntsen, Ø. A. (2016). A new level set numerical wave tank with improved density interpolation for complex wave hydrodynamics. *Computers & Fluids*, *140*, 191–208.

Fadlun, E., Verzicco, R., Orlandi, P., & Mohd-Yusof, J. (2000). Combined immersed-boundary finite-difference methods for three-dimensional complex flow simulations. *Journal of computational physics*, *161*(1), 35–60.

Goldstein, H., Poole, C., & Safko, J. (2001). Cpp, safko jl: Classical mechanics. *Addison-Wesley*, *6*, 5.

Jiang, G., & Peng, D. (2000). Weighted ENO schemes for Hamilton Jacobi equations. *SIAM Journal of Scientific Computing*, *Volume 21*, 2126–2143.

Jiang, G.-S., & Shu, C.-W. (1996). Efficient implementation of weighted eno schemes. *Journal of computational physics*, *126*(1), 202–228.

Kamath, A., Bihs, H., & Arntsen, Ø. A. (2017). Study of water impact and entry of a free falling wedge using computational fluid dynamics simulations. *Journal of Offshore Mechanics and Arctic Engineering*, *139*(3).

Katsidoniotaki, E., Shahroozi, Z., Eskilsson, C., Palm, J., Engström, J., & Göteman, M. (2023). Validation of a cfd model for wave energy system dynamics in extreme waves. *Ocean Engineering*, *268*, 113320.

Kempe, T., & Fröhlich, J. (2012). An improved immersed boundary method with direct forcing for the simulation of particle laden flows. *Journal of Computational Physics*, *231*(9), 3663–3684.

Kempe, T., Lennartz, M., Schwarz, S., & Fröhlich, J. (2015). Imposing the free-slip condition with a continuous forcing immersed boundary method. *Journal of Computational Physics*, *282*, 183–209.

Martin, T. (2021). A new cfd-based framework for modelling the interaction of open ocean aquaculture structures and complex free surface hydrodynamics.

Martin, T., A., T., & Bihs, H. (2021). numerical framework for modelling the dynamics of open ocean aquaculture structures in viscous fluids. *Applied Ocean Research*, *106*, 102410.

Miquel, A. M., Kamath, A., Alagan Chella, M., Archetti, R., & Bihs, H. (2018). Analysis of different methods for wave generation and absorption in a cfd-based numerical wave tank. *Journal of Marine Science and Engineering*, *6*(2), 73.

Osher, S., & Sethian, J. A. (1988). Fronts propagating with curvature-dependent speed: Algorithms based on Hamilton-Jacobi formulations. *Journal of Computational Physics*, *79*, 12–49.

Peng, D., Merriman, B., Osher, S., Zhao, H., & Kang, M. (1999). A PDE-based fast local level set method. *Journal of Computational Physics*, *155*, 410–438.

Peskin, C. S. (1972). Flow patterns around heart valves: a numerical method. *Journal of computational physics*, *10*(2), 252–271.

Shahroozi, Z., Göteman, M., & Engström, J. (2022). Experimental investigation of a point-absorber wave energy converter response in different wave-type representations of extreme sea states. *Ocean Engineering*, *248*, 110693.

Shivarama, R., & Fahrenthold, E. P. (2004). Hamilton's equations with euler parameters for rigid body dynamics modeling. *J. Dyn. Sys., Meas., Control*, *126*(1), 124–130.

Shu, C., & Osher, S. (1988). Efficient implementation of essentially non-oscillatory shock-capturing schemes. *Journal of Computational Physics*, *Volume 77(2)*, 439–471.

Sussman, M., Smereka, P., & Osher, S. (1994). A level set approach for computing solutions to incompressible two-phase flow. *Journal of Computational Physics*, *114*, 146–159.

Timmermans, L. J., Minev, P. D., & Van De Vosse, F. N. (1996). An approximate projection scheme for incompressible flow using spectral elements. *International journal for numerical methods in fluids*, *22*(7), 673–688.

Uhlmann, M. (2005). An immersed boundary method with direct forcing for the simulation of particulate flows. *Journal of Computational Physics*, *209*(2), 448–476.

van der Vorst, H. (1992). BiCGStab: A fast and smoothly converging variant of Bi-CG for the solution of nonsymmetric linear systems. *SIAM Journal of Scientific Computing*, *Volume 13*, 631–644.

Yang, L. (2018). One-fluid formulation for fluid–structure interaction with free surface. *Computer Methods in Applied Mechanics and Engineering*, *332*, 102–135.